

# Modeling the near-infrared lines of O-type stars

A. Lenorzer<sup>1</sup>, M. R. Mokiem<sup>1</sup>, A. de Koter<sup>1</sup>, and J. Puls<sup>2</sup>

<sup>1</sup> Astronomical Institute “Anton Pannekoek”, Kruislaan 403, 1098 SJ Amsterdam, The Netherlands

<sup>2</sup> Institut für Astronomie und Astrophysik, Universitätssternwarte, Scheinerstr. 1, 81679 München, Germany

Received 30 January 2004 / Accepted 30 March 2004

**Abstract.** We use a grid of 30 line-blanketed unified stellar photosphere and wind models for O-type stars; computed with the code CMFGEN in order to evaluate its potential in the near-infrared spectral domain. The grid includes dwarfs, giants and supergiants. We analyse the equivalent width behaviour of the 20 strongest lines of hydrogen and helium in spectral windows that can be observed using ground-based instrumentation and compare the results with observations. Our main findings are that: *i*) He I/He II line ratios in the *J*, *H* and *K* bands correlate well with the optical ratio employed in spectral classification, and can therefore be used to determine the spectral type; *ii*) in supergiant stars the transition from the stellar photosphere to the wind follows a shallower density gradient than the standard approach followed in our models, which can be mimicked by adopting a lower gravity in our prescription of the density stratification; *iii*) the Br $\gamma$  line poses a number of peculiar problems which might partly be related to wind clumping; and *iv*) the Br $\alpha$  line is an excellent mass-loss indicator. For the first and last item we provide quantitative calibrations.

**Key words.** stars: atmospheres – stars: early-type – stars: fundamental parameters - infrared: stars

## 1. Introduction

A large fraction of the galactic population of massive stars lies hidden behind tens of magnitudes of visual extinction. The reasons for this are that massive stars are so rare that their typical distances are a sizable fraction of the Galactic scale and that they are concentrated in the Galactic disk. Therefore, these stars suffer from obscuration by intervening molecular gas and dust clouds in the line-of-sight. Moreover, due to the short lifetimes of high-mass stars, they are located in star forming environments. As they typically form in the densest parts of these giant molecular clouds, they spend a significant fraction of their life embedded in this natal environment, before either moving out or breaking out.

Over the last decade several tens of massive stars were discovered in the near-infrared spectral window, where extinction by intervening dust is strongly reduced compared to the optical and ultraviolet window (Hanson et al. 2002; Kaper et al. 2002; Kendall et al. 2003). Studying the physical properties of these stars from their near-infrared radiation alone is essential (for instance in relation to their formation mechanism), but not an easy task. The *J*, *H*, *K*, and *L* spectral windows contain relatively few lines, mostly of hydrogen and helium. These lines are difficult to model as, for O-type stars, most near-infrared lines are formed in the transition region from the stellar photosphere (where the optical absorption spectrum originates) to

the super-sonic stellar wind (see e.g., Kudritzki & Puls 2000). This makes a treatment of the stellar wind an integral aspect of quantitative spectroscopic studies of O-type stars in the near-infrared, perhaps excluding late-type O V stars of which the stellar winds are relatively weak ( $\dot{M} \leq 10^{-7} M_{\odot} \text{ yr}^{-1}$ ). A fundamental problem is that so far we have only a poor knowledge of the way in which the density structure in the transition region and lower part of the wind (up to a few times the sonic velocity) behaves. Though the basic driving mechanism of stellar winds has been identified (e.g., Castor et al. 1975; Abbott 1982; Pauldrach et al. 1986) a fully self-consistent numerical implementation of radiative line-driving is, at present, not feasible for models which have been constructed for the objective of atmospheric analyses. Moreover, the inevitable assumptions made in describing this theory are anticipated to have severe effects on the physics of the transition region. As an example, the neglect of line source-function gradients when using the Sobolev approximation might lead to erroneous values for the radiative acceleration just in this transition region, at least in the case of thin winds (cf. Owocki & Puls 1999).

One may identify two essentially complementary approaches for making progress in the development of near-infrared diagnostics that allow for a characterisation of the basic stellar and wind properties of O-type stars. The first is to establish the near-infrared spectroscopic characteristics of O stars with known properties from studies at other wavelengths. One may then try to correlate the behaviour of these lines with their basic properties and see if one can retrieve

the same information. This requires high-quality near-infrared spectra of a large sample of MK standard stars. So far, a good coverage is available only for the 2.0–2.2  $\mu\text{m}$  range (see Hanson et al. 1996, 2003). The second approach is to model the near-infrared lines using state of the art techniques, and then to study the dependence between spectral and basic properties.

So far modelling of the near-infrared spectral region has been done for extreme early-type stars, i.e., Luminous Blue Variables (Najarro et al. 1997), Of/WN stars (Crowther et al. 1995) and galactic centre objects (Najarro et al. 1994). This study aims at an improved treatment of normal O stars. With the use of sophisticated models that include a detailed treatment of stellar winds and that properly describe the spectrum, we study the predictions for the near-infrared regime. We investigate to what extent the near-infrared lines can be used to determine the spectral type, luminosity class, and mass loss of O-type stars, focussing on lines that are observable using ground-based instrumentation.

This paper is organized as follows: in Sect. 2 we introduce our grid of models. Predicted equivalent widths ( $EW$ ) of near-infrared lines are presented and their dependence on model parameters are discussed in Sect. 3. Model prediction are compared with observations gathered from the literature in Sect. 4. In Sect. 5, we present near-infrared spectral classification schemes for O-type stars and a means to determine wind properties. We end with conclusions.

## 2. The grid of models

For this study we employ a grid of unified stellar photosphere and wind models for O-type stars of luminosity class V, III and Ia. This grid was constructed using the CMFGEN program of Hillier & Miller (1998), to which we refer for a full description. In short: CMFGEN solves the equations of radiative transfer subject to the constraints of statistical equilibrium, for an atmosphere with an outflowing stellar wind. The ions included in the non-LTE calculations are H I, He I–II, C III–IV, N III–V, O III–VI, Si IV and Fe III–VII, accounting for a total of approximately 20 000 bound-bound transitions. These reflect some 30 000 lines and ensure a self-consistent treatment of line blanketing, i.e., the cumulative effect of the spectral lines, especially iron, on the stellar atmosphere.

The grid consists of 30 models ranging in effective temperature,  $T_{\text{eff}}$ , from  $\sim 24\,000$  K up to  $\sim 49\,000$  K, with 10 models for each luminosity class. The stellar parameters are shown in Table 1, with masses derived from evolutionary tracks. For the basic stellar parameters we employed the calibration from Vacca et al. (1996), which is based on a set of plane parallel non-LTE H and He models that do not account for line-blanketing. In the case of the last two models in the dwarf and giant class and for the last three models in the supergiant class the parameters were derived by extrapolating the relations found by these authors for  $T_{\text{eff}}$ ,  $\log g$  and  $M_V$ . For the stellar radius we adopt the radius at which  $\tau(R_\star) = 2/3$ , with  $\tau(r)$  being the mean Rosseland optical depth corrected for geometrical dilution (Eq. (4) from Lucy 1976). This does not exactly coincide with the radius give by Vacca et al. However, the

correction is minor and at most half a percent. To be consistent we have included this correction in the values of  $T_{\text{eff}}$  and  $\log g$  in Table 1. For the supergiant models, we also calculated a grid with gravities based on the (lower) spectroscopic masses (see Vacca et al. 1996), in order to investigate the dependence of the near-infrared lines on  $\log g$  (see e.g., Herrero et al. 1992). For the chemical composition solar abundances from Cox (2000) were incorporated, which are listed in the caption of Table 1. Note in particular that our model grid comprises “only” models with “normal” helium content, which has to be considered when comparing our results with observations later on. The reader should also note that the  $\log g$  values of the luminosity class V models in Table 1 do not reflect ZAMS values. On the ZAMS there is a small negative correlation between mass and  $\log g$  (e.g., Schaller et al. 1992). In the empirical calibration from Vacca et al. this is reversed. However, for the major objective and results of this study this has no influence.

The density structure in the photosphere is based on hydrostatic equilibrium in an isothermal medium of temperature  $T_{\text{eff}}$ . In that case the density scale height is given by

$$H = \frac{kT_{\text{eff}}}{\mu m_{\text{amu}} g_{\text{eff}}}, \quad (1)$$

where  $\mu$  is the mean molecular weight in atomic mass units ( $m_{\text{amu}}$ ) and  $g_{\text{eff}}$  is the gravity at the stellar surface corrected for radiation pressure by electron scattering. The density structure near and beyond the sonic point is set by the velocity law through the equation of mass-continuity. This velocity structure is given by a standard  $\beta$ -law, which is smoothly connected to the photosphere. The value of  $\beta$  is set to 0.8 for the dwarfs and to 1.0 for the giant and super giants, as these stars have a tendency toward higher  $\beta$  (e.g., Groenewegen & Lamers 1989; Puls et al. 1996). The terminal wind velocity  $v_\infty$  follows from a scaling with the escape velocity  $v_{\text{esc}}$  (Abbott 1982; Lamers et al. 1995). For stars with spectral type earlier than approximately B2 this scaling implies that the ratio  $v_\infty/v_{\text{esc}}$  is 2.6. Stars with a later spectral type have a ratio of 1.3. This discontinuity is referred to as the bi-stability jump and implies a larger mass-loss rate and lower wind velocity for stars at the cool side of this jump. This is the case for the coolest model in our grid, Model 10 Ia. The mass-loss rates incorporated in the models are from the theoretical predictions by Vink et al. (2000, 2001). These are listed in Table 1 together with the terminal velocities.

In the statistical equilibrium and radiative transfer calculation a micro turbulent velocity of  $v_{\text{turb}} = 20 \text{ km s}^{-1}$  was assumed for all lines. In the formal solution of the radiative transfer equation, yielding the emergent spectrum, we assumed micro turbulent velocities of 10 and 20  $\text{km s}^{-1}$  (see e.g., Smith & Howarth 1998; Villamariz & Herrero 2000). Apart from the broadening due to thermal motions and micro turbulence, Stark broadening tables for H, He I and He II lines were included.

As the effective temperature scale for O-type stars is currently being revised using different models all accounting for line-blanketing (e.g. de Koter et al. 1998; Martins et al. 2002; Repolust et al. 2004), the spectral types attributed by Vacca et al. (1996) cannot be applied to our models. Instead we use as a quantitative criterion the ratio of the equivalent widths

**Table 1.** Stellar and wind parameters of our model grid. For supergiants, we list  $\log g$  values derived for both the spectroscopic and evolutionary mass. Values of  $T_{\text{eff}}$  and  $R_{\star}$  for supergiants correspond to models with evolutionary masses. Adopted abundances by mass fraction are from Cox (2000): H = 0.7023, He = 0.2820, and, in units of  $10^{-3}$ , C = 3.050, N = 1.100, O = 9.540, Si = 0.699, Fe = 1.360.

Luminosity class V											
Model	$T_{\text{eff}}$ (K)	$\frac{M_{\star}}{M_{\odot}}$	$\frac{R_{\star}}{R_{\odot}}$	$\log g$ ( $\text{cm s}^{-2}$ )	$\log\left(\frac{L_{\star}}{L_{\odot}}\right)$	$H_{\star}$ ( $10^{-4} R_{\star}$ )	$\log \dot{M}$ ( $M_{\odot}/\text{yr}$ )	$\beta$	$v_{\infty}$ ( $\text{km s}^{-1}$ )		
1V	48 618	68.9	12.3	4.094	5.882	8.308	-5.375	0.8	3240		
2V	46 070	56.6	11.4	4.075	5.722	8.375	-5.599	0.8	3140		
3V	43 511	45.2	10.7	4.032	5.568	8.971	-5.805	0.8	2950		
4V	40 964	37.7	10.0	4.012	5.404	9.046	-6.072	0.8	2850		
5V	38 406	30.8	9.3	3.987	5.229	9.314	-6.369	0.8	2720		
6V	35 861	25.4	8.8	3.951	5.062	9.712	-6.674	0.8	2570		
7V	33 306	21.2	8.3	3.924	4.883	9.934	-7.038	0.8	2450		
8V	32 028	19.3	8.0	3.915	4.783	9.988	-7.252	0.8	2400		
9V	30 820	17.7	7.8	3.897	4.697	10.16	-7.445	0.8	2330		
10V	28 270	14.8	7.4	3.864	4.502	10.40	-7.913	0.8	2210		
Luminosity class III											
1III	48 132	82.8	15.1	3.996	6.042	9.098	-5.125	1.0	3080		
2III	45 363	68.4	15.0	3.919	5.934	10.04	-5.239	1.0	2850		
3III	42 595	56.6	14.8	3.848	5.813	10.82	-5.397	1.0	2660		
4III	39 815	47.4	14.7	3.777	5.690	11.53	-5.585	1.0	2490		
5III	37 049	39.0	14.7	3.692	5.564	12.63	-5.791	1.0	2290		
6III	34 282	32.6	14.7	3.614	5.430	13.50	-6.051	1.0	2130		
7III	31 504	27.4	14.7	3.539	5.283	14.20	-6.377	1.0	1990		
8III	30 127	25.1	14.8	3.495	5.211	14.69	-6.551	1.0	1920		
9III	28 781	23.5	14.8	3.464	5.134	14.73	-6.758	1.0	1870		
10III	26 011	20.2	15.0	3.386	4.970	15.18	-7.230	1.0	1750		
Luminosity class Ia											
1Ia	47 641	104.7	55.9	18.6	3.916	3.639	6.206	9.502	-4.896	1.0	3000
2Ia	44 642	86.5	48.6	19.6	3.788	3.533	6.139	11.63	-4.922	1.0	2620
3Ia	41 651	74.7	42.5	20.6	3.681	3.431	6.062	12.95	-5.014	1.0	2400
4Ia	38 663	64.3	37.4	21.8	3.566	3.327	5.981	14.44	-5.134	1.0	2190
5Ia	35 673	54.8	33.1	23.1	3.446	3.223	5.892	16.15	-5.295	1.0	1990
6Ia	32 687	46.7	29.5	24.6	3.322	3.120	5.795	17.90	-5.509	1.0	1810
7Ia	31 194	43.1	27.9	25.4	3.260	3.068	5.741	18.70	-5.644	1.0	1730
8Ia	29 719	40.9	26.0	26.2	3.211	3.012	5.683	18.67	-5.815	1.0	1690
9Ia	26 731	36.1	23.7	28.1	3.094	2.909	5.563	19.35	-6.202	1.0	1570
10Ia	23 733	32.4	22.0	30.5	2.976	2.805	5.427	19.53	-5.409	1.0	740

of the He I  $\lambda 4471$  and He II  $\lambda 4542$  lines from Mathys (1988). This enables us to unambiguously assign spectral types to our models.

## 2.1. Limitations of the models

Though the models presented in this study are state-of-the-art, they do (inevitably) contain a number of assumptions. With

respect to the prediction of the near-infrared spectrum the most important ones are:

### 2.1.1. A constant photospheric scale height

We assume a constant density scale height to describe the density structure in the stellar photosphere (see Eq. (1)). In reality, the run of density in this regime follows from the equation of hydrostatic equilibrium, i.e. it takes into account the

exact temperature structure, the radiative pressure (from continua and lines) as well as changes in the mean molecular weight. The lines that are expected to be affected the most by this assumption are optical lines that are sensitive to density, most notably the wings of Balmer lines. These lines are used to derive the stellar gravity. Gravity determinations based on these lines may therefore lead to a systematic overestimate of  $\log g$  of up to 0.10 to 0.15 dex (F. Najarro, private communication). This effect is less important for the strong near-infrared lines and especially for supergiant models in which these lines are mainly formed beyond the photosphere.

### 2.1.2. The density structure in the transition zone

A proper treatment of the density structure in the transition region between the photosphere and the super-sonic wind requires solving the equation of motion, taking into account all processes that are responsible for the acceleration of the stellar outflow. Most important, one should account for effects of radiation pressure on spectral lines. This problem is at present too complex to be solved for self-consistently in our models. Our approach is to adopt a simple, empirical description of the density stratification in this region, i.e. we smoothly connect the exponential increase of velocity in the photosphere to a beta-type velocity law in the supersonic regime. This is achieved by taking

$$v(r) = \frac{(v_{\infty} + (v_{\infty} - v_{\circ})(1 - R/r)^{\beta})}{(1 + (v_{\circ}/v_{\text{core}})\exp([R - r]/H))}, \quad (2)$$

where  $v_{\text{core}}$  is the velocity at the inner boundary of the model, and which, by means of the mass-continuity relation, sets the density at  $R_{\text{core}}$ . Typically, this density is chosen sufficiently high to assure full thermalisation of the radiation field. The velocity parameter  $v_{\circ}$  is used to assure a smooth transition from the photosphere to the supersonic wind. The latter is prescribed by the terminal velocity  $v_{\infty}$  and the parameter  $\beta$ , essentially defining the steepness of the velocity law near and beyond the sonic point.

An important outcome of this study is the ability to check whether this commonly used representation of the density structure is able to reproduce the properties of near-infrared lines, which are typically formed in the transition region and/or lower part of the wind. The major part of the discrepancies between observations and predictions of these lines can likely be ascribed to shortcomings of the above description.

### 2.1.3. Clumping

There is evidence that the stellar winds of early-type stars are inhomogeneous on small length scales. Observational evidence exists for Wolf-Rayet stars (Robert 1994; Hillier 1991) as well as for some O-type stars (e.g. Eversberg et al. 1998; Bouret et al. 2003). Theoretical indications for this effect are provided by Owocki et al. (1988). One may anticipate that in clumped winds strong infrared lines such as Br $\alpha$  and Br $\gamma$  and possibly Pf $\gamma$  and He II (6–7) will be affected the most. For recombination lines clumping effects introduce a degeneracy in

the quantity  $\dot{M}/\sqrt{f}$ , where  $f$  is the clumping factor defined as  $\bar{\rho} = f\rho$ . Here it is assumed that the inter-clump medium is void, and that  $\bar{\rho}$  is the unclumped wind density. Lines of varying strength may be affected in different ways if the clumping factor depends on radial distance. Potentially, the behaviour of the strong near-infrared lines may yield constraints on the clumping properties. As we want to focus on other parameters in this first study, we adopt an unclumped medium in our models.

### 2.1.4. Turbulence

In our models we assume a constant microturbulent velocity throughout the photosphere and wind. On the basis of Br $\alpha$  and Pf $\alpha$  observations Zaai et al. (2001) found evidence for a gradient in the turbulent velocity in the outer photospheres of late-O and early-B dwarfs and giants. Such an increase in micro turbulence with radial distance may also be present in O stars of earlier spectral type.

## 2.2. Optical line trends

Before using our grid of models to investigate near-infrared lines, we present their predictions for the two optical lines used for spectral classification. Predicted  $EW$  are compared with observations gathered from the literature and are shown in Fig. 1. The general trends are well reproduced by the models, the largest deviation being that the He II line is slightly overestimated in dwarf models. This discrepancy is also present in the grid of dwarf star CMFGEN models presented by Martins et al. (2002). The grid of models covers most of the span in equivalent width present in the observations. This is not the case, however, when considering each luminosity class separately. Indeed, stars with similar spectral type and luminosity class show a range of stellar and wind parameters introducing a scatter in the observed line  $EW$ . Furthermore variations in metallicity and stellar rotation are not taken into account in our grid, but are also a source of scatter. Still, the grid is suited for global studies of basic parameters and is used for this purpose in the following sections.

## 3. Near-infrared line trends

Before presenting our results, let us point out some principal problem arising in (near) IR line formation (see also Mihalas 1978; Kudritzki 1979; Najarro et al. 1998; Zaai et al. 1999). Because  $h\nu/kT \ll 1$  in the IR, stimulated emission becomes important, and deviations from LTE in the line might become substantially amplified, compared to the UV/optical case. Let  $\delta = b_1/b_u - 1$ , with non-LTE departure coefficients  $b_1$  and  $b_u$  for the lower and upper level of the considered transition. By expansion, we then find for the IR line source function (in units of the Planck-function)

$$\frac{S_{\text{line}}^{\text{IR}}}{B_{\nu}} \approx \frac{1}{1 + \delta + \delta \frac{kT}{h\nu}}, \quad \frac{h\nu}{kT} \ll 1, \quad (3)$$

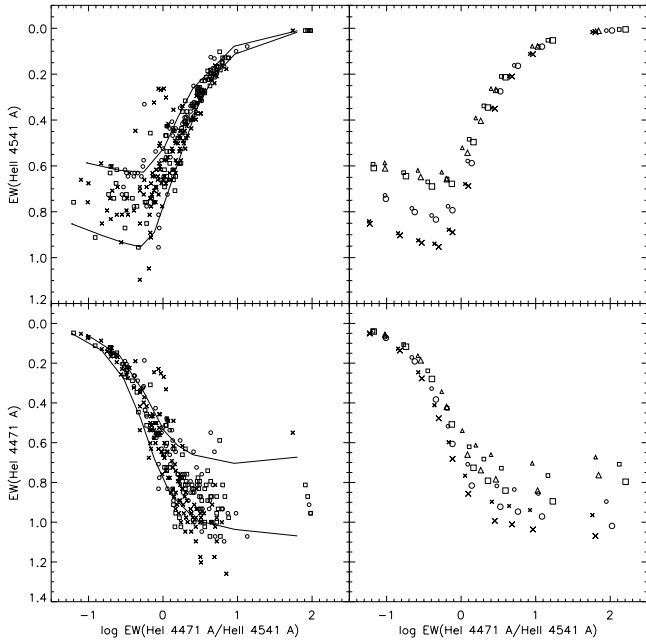


**Fig. 1.** *Left:* observed  $EW$  (in  $\text{\AA}$ ) from Mathys (1988, 1989), Conti & Alschuler (1971), Conti & Frost (1977), Bisiacchi et al. (1982) are plotted with crosses for dwarfs, circles for giants and squares for supergiants. Typical errors in the observations are 5 to 10%. The solid lines show the maximum and minimum values predicted in our models. *Right:* equivalent width predictions for He I are plotted for dwarfs (crosses), giants (circles), supergiants (squares) and lower surface gravity supergiants (triangles). Small symbols are for a turbulent velocity of  $10 \text{ km s}^{-1}$ , large symbols for turbulent velocity of  $20 \text{ km s}^{-1}$ .

compared to the corresponding expression in the UV,

$$\frac{S_{\text{line}}^{\text{UV}}}{B_{\nu}} \approx \frac{1}{1 + \delta}, \quad \frac{h\nu}{kT} \gg 1. \quad (4)$$

In typical cases with  $\lambda = 2 \mu\text{m}$  and  $T = 30\,000 \text{ K}$ , we thus have

$$\frac{S_{\text{line}}^{\text{IR}}}{B_{\nu}} \approx \frac{1}{1 + 5\delta}.$$

If now the upper level becomes overpopulated with respect to the lower one (as it is typical for some IR transitions),  $\delta$  is negative, and the line source function can become much larger than the Planck-function, leading to strong emission already for relatively low wind densities. Even more important (and problematic), however, is the fact that the response of the source function on small changes in the population number ratio is much stronger than in the UV/optical case. This means that small effects on the occupation numbers can have substantial effects on the synthesized lines, and that apparently large discrepancies between theory and observations may be caused by relatively small inconsistencies. We will come back to this problem when confronting our results for  $\text{Br}\gamma$  with observations.

After this introductory remark, we will now present our equivalent width ( $EW$ ) predictions for the strongest hydrogen and helium lines in the near infrared, and discuss their dependence on model parameters. The lines are listed in Table 2, together with blends present in the wings of their profiles that are included in the  $EW$  predictions. In the following a positive and

**Table 2.** Identification of the lines used in this study.

Line	Transition	Wavelength $\mu\text{m}$	Lines comprised in $EW$ measurement
$\text{Pa}\beta$	3–5	1.2822	He II (6–10) $\lambda 1.2816$ He I (3p–5s) $\lambda 1.2849$ He I (3d–5f) $\lambda 1.2788$ C III $\lambda 1.2794$
$\text{Pa}\gamma$	3–6	1.0941	He II (6–12) $\lambda 1.0936$ He I (3d–6f) $\lambda 1.0916$ C III $\lambda 1.0920$
$\text{Br}\alpha$	4–5	4.0523	He II (8–10) $\lambda 4.0506$ He I (4f–5g) $\lambda 4.0409$ He I (4f–5g) $\lambda 4.0377$
$\text{Br}\gamma$	4–7	2.1661	He II (8–14) $\lambda 2.1652$
Br 10	4–10	1.7367	
Br 11	4–11	1.6811	
$\text{P}\gamma$	5–8	3.7406	
Pf9	5–9	3.2970	
Pf 10	5–10	3.0392	
He II	5–7	1.1630	
He II	6–7	3.0917	He II (8–11) $\lambda 3.0955$ C III $\lambda 3.0878$ C III $\lambda 3.0843$ C III $\lambda 3.0763$
He II	6–11	1.1676	
He II	7–10	2.1891	
He II	7–12	1.6923	
He II	7–13	1.5722	
He I	2s–2p	2.0587	
He I	3p–4s	2.1126	
He I	3p–4s	2.1138	
He I	3p–4d	1.7007	
He I	3p–5d	1.1972	
He I	3d–5f	1.2788	
He I	4p–5d	3.7036	
C IV	3d–3p	2.0802	
C III	7–8	2.1151	

negative  $EW$  correspond, respectively, to an absorption line and an emission line.

### 3.1. Hydrogen lines

The near-infrared domain includes several hydrogen lines from different series: Paschen in the  $J$  band, Brackett in the  $H$ ,  $K$  and  $L$  band and Pfund in the  $L$  band. Higher members of the Pfund and Humphreys series are also located in the  $K$

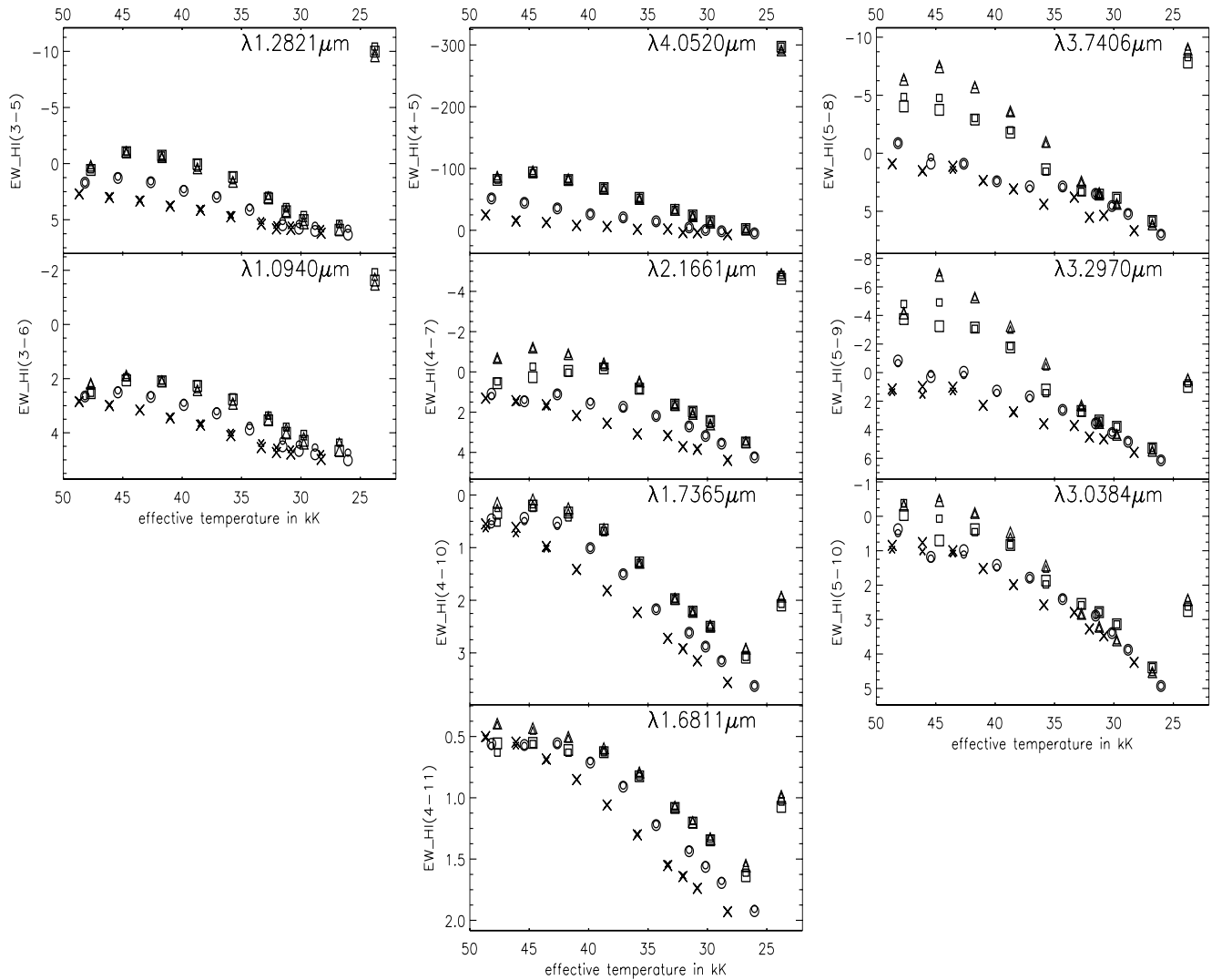


**Fig. 2.** Equivalent width predictions (in Å) for hydrogen lines are plotted for dwarfs (crosses), giants (circles), supergiants (squares) and lower surface gravity supergiants (triangles). Small symbols are for a turbulent velocity of  $10 \text{ km s}^{-1}$ , large symbols for a turbulent velocity of  $20 \text{ km s}^{-1}$ .

and  $L$  band, respectively. A high density and a low hydrogen ionisation fraction are required to make them observable. Although this is the case for cooler stars and emission line stars, these lines are not reported in the spectra of O-type stars and are not included in our model calculations which include 13 levels of hydrogen.

We plotted  $EW$  predictions of the Paschen, Brackett and Pfund lines for all models in Fig. 2. The  $Br\alpha$  line is blended with the  $He\text{I}(4f-5g)$  and  $He\text{II}(8-10)$  lines in all spectra, and with  $He\text{I}(4d-5f)$  for models with large wind velocities and mass-loss rates. We defined the  $EW$  of  $Br\alpha$  over the interval from  $4.0$  to  $4.1 \mu\text{m}$ , which includes these blends.  $Pa\beta$  and  $Pa\gamma$  lines are integrated over an interval that comprises the  $He\text{I}$  lines  $(3d-5f)$  and  $(3p-5s)$ , and  $(3d-6f)$ , respectively. The lines decrease in equivalent width with temperature in the range  $25$  to  $45 \text{ kK}$ . This trend is steeper for higher series, as well as for stronger lines within a series and for lines in supergiants relative to other luminosity classes. The lines show

progressively lower equivalent widths for decreasing luminosity class.

Two models do not follow this general trend: the hottest (1 Ia) and coolest (10 Ia) supergiant models computed in this study. In Model 10 Ia, the hydrogen lines have a more negative equivalent width compared to neighbouring models whereas it is the opposite in Model 1 Ia. This behaviour can be traced back to the adopted wind parameters. Model 10 Ia is at the cool side of the bi-stability jump, where it has a higher wind density (see Sect. 2). Model 1 Ia has a lower wind density than Model 2 Ia. The strongest lines show the most pronounced emission, as their line forming region extends further out in the wind. Differences with luminosity class are smaller for photospheric lines (e.g.  $Br\ 11$ ,  $Br\ 10$ ,  $Pf\ 10$ ). Their behaviour is mostly sensitive to temperature, and can therefore be used to constrain the spectral type. This also holds for  $Pa\beta$ ,  $Pa\gamma$ ,  $Br\gamma$  and  $Pf\gamma$ , except for supergiants, which have large mass-loss rates affecting also the  $\beta$  and  $\gamma$  lines.

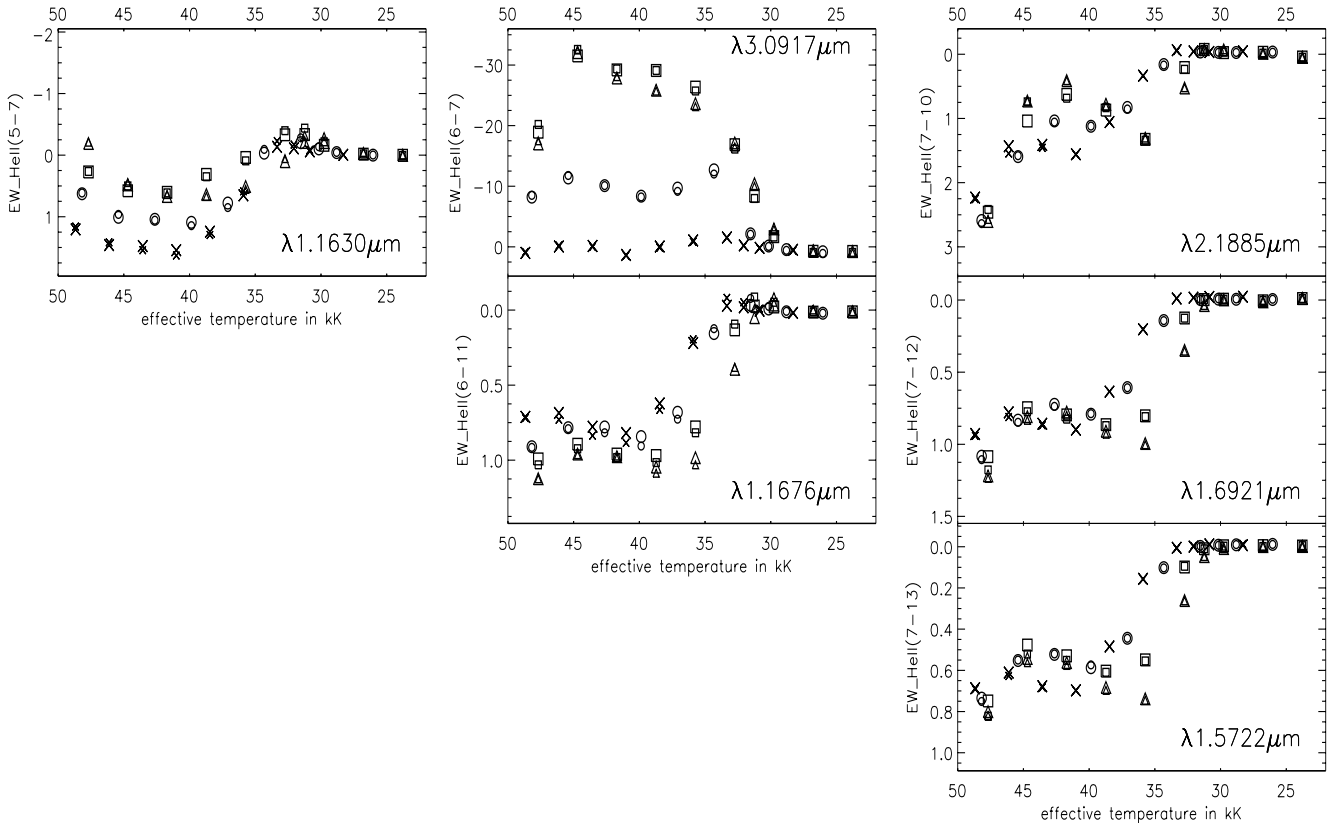


**Fig. 3.** Equivalent width predictions (in Å) for He II lines are plotted for dwarfs (crosses), giants (circles), supergiants (squares) and lower surface gravity supergiants (triangles). Small symbols are for a turbulent velocity of  $10 \text{ km s}^{-1}$ , large symbols for turbulent velocity of  $20 \text{ km s}^{-1}$ .

The two grids of supergiant models show that the Pfund lines and Br $\gamma$  are sensitive to the surface gravity. As these lines form in the region above the photosphere, but below the sonic point, they are sensitive to changes in gravity. The strong Br $\alpha$  line is formed in a much more extended region, i.e. also in the wind where the density structure is set by the velocity law, and is less sensitive to gravity effects. We have also investigated the effects of micro turbulence: as only the micro turbulent velocity in the calculation of the formal solution was modified, the occupation numbers are not influenced. Only the line profiles are additionally broadened. For the lines considered, the EWs differ only marginally between the two adopted turbulent velocities ( $10$  and  $20 \text{ km s}^{-1}$ ).

The strength of most predicted near-infrared hydrogen lines show a smooth behaviour as a function of model parameters. On top of this, the Pfund lines, and to a lesser extent Br $\gamma$ , show small model to model fluctuations. These may be intrinsic in nature (e.g. blends) or the result of numerical effects (e.g. sampling of the radius grid) and do not significantly affect our results.

### 3.2. He II lines

Several He II lines are present in the different observational bands. The strongest are the (5–7) and (6–11) transitions in the *J* band, (7–12) and (7–13) in the *H* band, (7–10) in the *K* band and (6–7) and in the *L* band. The behaviour of these lines can be split into three regimes following the ionisation of He II. The lines first appear at about 30 kK and increase in

absorption strength up to  $\sim 40 \text{ kK}$ . The exact temperature of this maximum absorption depends on gravity, ranging from 41 kK for dwarfs to 36 kK for supergiants. For temperatures  $T_{\text{eff}} \gtrsim 45 \text{ kK}$ , the lines weaken again. All high-temperature models show He II profiles in which the line core is reverted in emission, as a result of a temperature inversion in the line forming region. A temperature inversion is not present in the highest  $T_{\text{eff}}$  models. These therefore show normal absorption profiles. This explains the increased absorption seen in these hottest models. In giants and supergiants the strong  $\alpha$  line (6–7) at  $\lambda 3.0917 \mu\text{m}$  is formed in the stellar wind causing a strong emission profile. For the hottest supergiant model the line shows a decrease in emission that is the result of a lower wind density (as discussed in Sect. 3.1). The behaviour of He II  $\lambda 3.0917$  is complex as it is blended with the (8–11) line, which shows a singular behaviour as a result of it being interlocked with the (6–7) transition. For those cases where the (6–7) line is in emission, the (8–11) line is in absorption, while for an absorption profile for (6–7) the blending line is in emission. All luminosity classes suffer from this blending effect, however, for the supergiants the (6–7) dominates the equivalent width in such a way that no dip in EW occurs at  $\sim 41 \text{ kK}$ . Wind emission is also important for the (5–7) line.

The relatively weak He II lines may serve as temperature indicators, whereas the stronger lines are mostly sensitive to luminosity class, similar to hydrogen lines. For temperatures between 33 and 42 kK these lines are also sensitive to gravity. Like for the hydrogen lines, effects of micro turbulence are relatively modest.

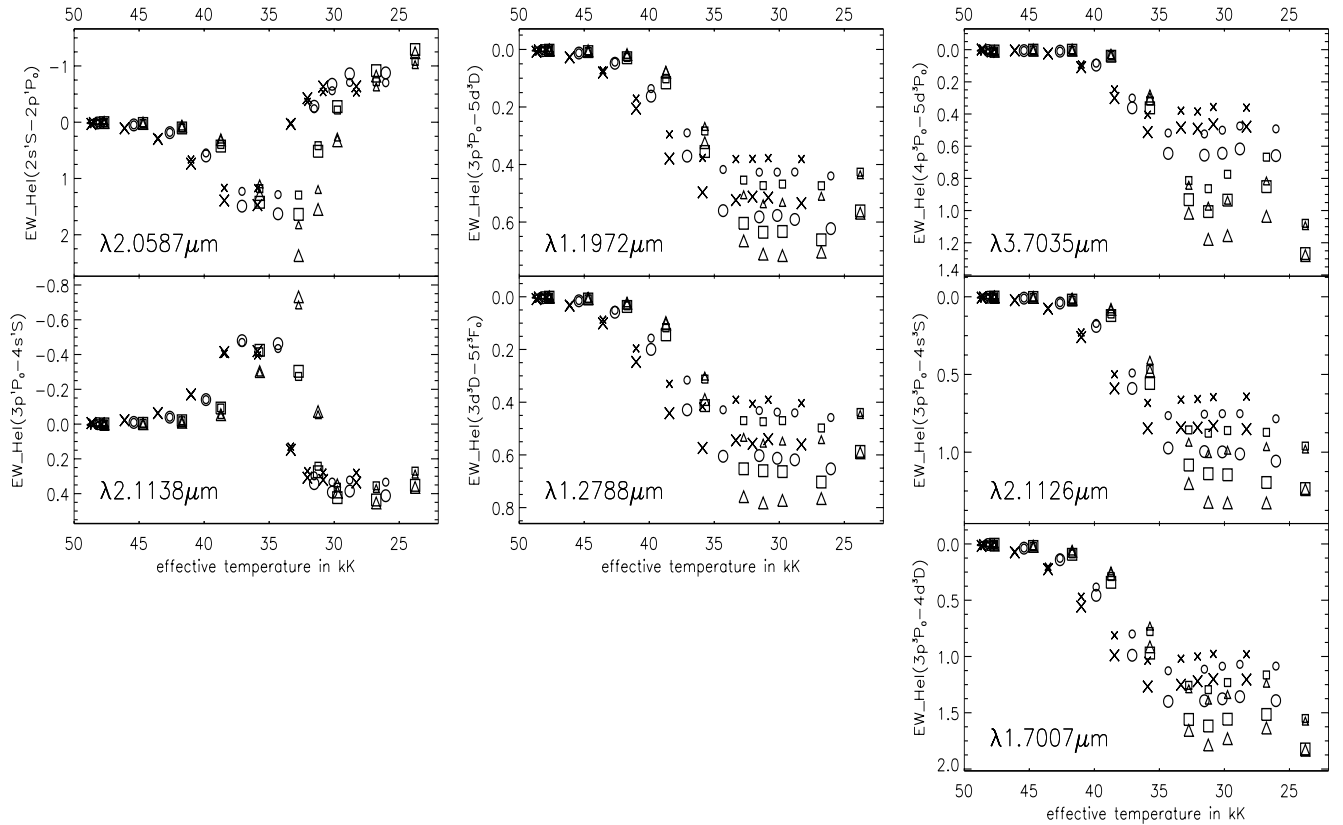


**Fig. 4.** Equivalent width predictions (in Å) for He I are plotted for dwarfs (crosses), giants (circles), supergiants (squares) and lower surface gravity supergiants (triangles). Small symbols are for a turbulent velocity of  $10 \text{ km s}^{-1}$ , large symbols for turbulent velocity of  $20 \text{ km s}^{-1}$ .

### 3.3. He I lines

Numerous He I lines are present in the near-infrared. Six of them were observed in the J band spectrum of a B0 Ia star by Wallace et al. (1997). We concentrate on the strongest lines present at  $\lambda 1.1972$  and  $1.2788 \mu\text{m}$  in the J band, at  $\lambda 1.7007$  in the H band, at  $\lambda 2.0587$ ,  $2.1126$  and  $2.1138$  in the K band, and at  $\lambda 3.7036 \mu\text{m}$  in the L band. The line trends are plotted in Fig. 4.

We first discuss the triplet transitions. These show a normal excitation and ionization behaviour, producing a broad peak in absorption strength near  $\sim 30 \text{ kK}$ . For higher temperatures the lines weaken, and disappear somewhere between 40 and  $50 \text{ kK}$ . Lines are weaker in lower gravity models that have  $T_{\text{eff}} \geq 35 \text{ kK}$ , a situation that is reversed at lower temperatures. The lines at  $\lambda 1.7007$ ,  $2.1126$  and  $3.7036 \mu\text{m}$  are the most sensitive to gravity. For a higher microturbulent velocity the equivalent width of the He I lines increases, as expected. We note that for the lines at  $\lambda 1.1972$ ,  $1.2788$  and  $3.7035 \mu\text{m}$  we do not have Stark broadening tables available, implying we underestimate the strength of these lines. The neglect of pressure broadening also explains why these lines appear more affected by a change in turbulence.

The singlet lines at  $\lambda 2.0587$  and  $2.1138 \mu\text{m}$  show a very different behavior as a result of a strong coupling to the strength of the ultraviolet line-blanketed continuum through the resonance transitions at  $584 \text{ \AA}$  and  $537 \text{ \AA}$  (see Najarro et al. 1994). The first transition reaches the upper level of the  $\lambda 2.0587$  line,

the second one that of the lower level of the  $\lambda 2.1138$  line. This causes the “inverted” behaviour of these two lines as seen in Fig. 4. The weakening of both lines at  $T_{\text{eff}} \geq 35 \text{ kK}$  is the result of progressive ionisation. The exact location of this peak absorption strength (for He I  $\lambda 2.0587$ ) and peak emission strength (for He I  $\lambda 2.1138$ ) depends somewhat on gravity, but ranges from  $38 \text{ kK}$  for dwarfs to  $33 \text{ kK}$  for supergiants.

Most of the He I lines discussed are expected to be useful temperature diagnostics, especially at temperatures beyond  $\sim 35 \text{ kK}$ . At lower  $T_{\text{eff}}$  the lines show a strong dependence on gravity and/or turbulent velocity.

## 4. Comparison with observations

Calibration of the trends predicted by the models requires a large data set of near-infrared spectroscopic observations of O-type stars with well known properties obtained from optical and ultraviolet studies. Observations of near-infrared lines are still scarce, although some effort has been made in this direction over the last decade. In particular, we make use of the K-band atlas of Hanson et al. (1996), the H-band collection of spectra of Hanson et al. (1998) and the ISO/SWS atlas of Lenorzer et al. (2002a) covering the L-band. Additional measurements were gathered from Blum et al. (1997) and Zaal et al. (2001) for the He I line at  $\lambda 1.7007$  and the Br $\alpha$  line, respectively. This collection of observations allows a first limited comparison with models. Observed equivalent widths are plotted in Fig. 5 together with the model trends. These trends give

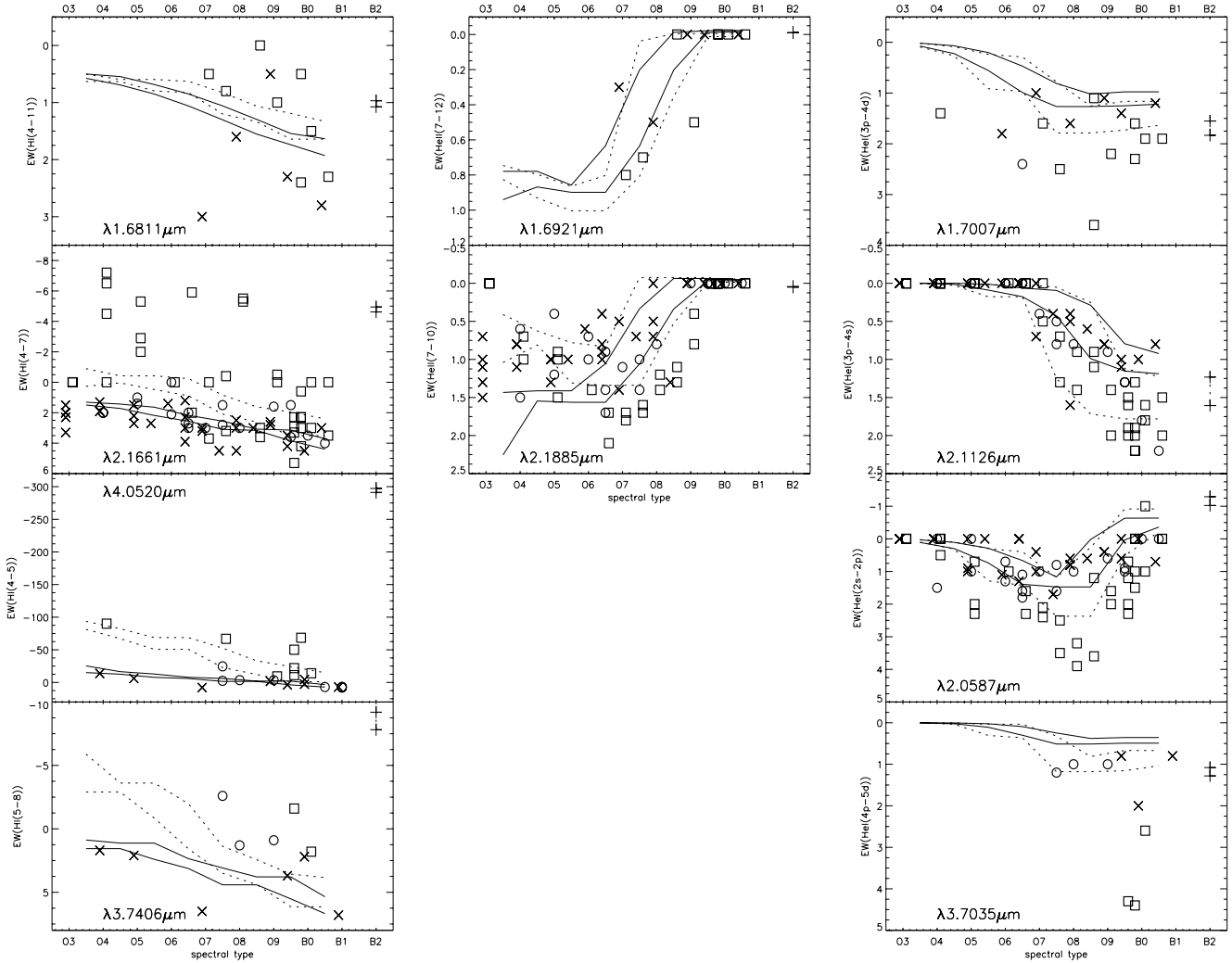


**Fig. 5.** The maximum and minimum  $EW$  predictions (in  $\text{\AA}$ ) are plotted for dwarf (solid lines), and supergiant (dotted lines) models. Models beyond the bi-stability jump are denoted by pluses. Observations from Hanson et al. (1996); Blum et al. (1997); Hanson et al. (1998); Zaai et al. (2001) and Lenorzer et al. (2002a) are plotted with crosses for dwarfs, circles for giants and squares for supergiants. Typical error on the observations is  $\pm 0.5 \text{\AA}$ .

the minimum and maximum  $EW$  values for the dwarf (solid lines) and supergiant models (dotted lines), assuming that the spectral types attributed to the models are accurate to within one subtype.

Considering the hydrogen lines (left panel), the general trends are fairly well reproduced by the models, though the observations of lines affected by the stellar wind ( $\text{Br}\alpha$ ,  $\text{Br}\gamma$ ) show a much larger scatter than is produced by the range of parameters that we have investigated.

#### 4.1. The $\text{Br}\gamma$ problem

The line for which a large observed scatter is clearly seen is  $\text{Br}\gamma$ . Note that the only model in the  $\text{Br}\gamma$  panel that produces an emission equivalent width that is comparable to the highest values that are observed is the one for the coolest  $T_{\text{eff}}$  (represented by a plus sign). This model is at the cool side of the bi-stability jump and has a much higher wind density. One would expect a range of wind densities in O-type supergiants of given spectral type, as these show a considerable spread in luminosity (and therefore mass loss). The observations,

however, lie systematically above the prediction of typical Ia stars. This may either suggest a strong underprediction of the wind density (which seems unlikely on the basis of optical and ultraviolet studies) or that clumping of the stellar wind is important for near-infrared wind lines. A clumped medium would lead to an increase of the emission line strength, as clumping results in an increased recombination rate inside the clumps and in an enhanced optical depth ( $\langle \rho^2 \rangle > \langle \rho \rangle^2$ ). Although this seems to be a plausible argument,  $\text{Br}\gamma$  poses two additional problems. Note at first that due to the lower oscillator strength and the lower occupation numbers,  $\text{Br}\gamma$  should form *inside* the  $\text{H}\alpha$  emitting volume (the  $gf$ -value of  $\text{Br}\gamma$  lies in between the  $gf$ -values of  $\text{H}\alpha$  and  $\text{H}\beta$ ). Actually, for almost all of our models it turned out that  $\text{Br}\gamma$  is formed in the same region as  $\text{H}\beta$ . Since this region lies close to the sonic one, the degree of clumping should be small. Second, our synthetic  $\text{Br}\gamma$  lines for stronger winds display well developed P Cygni type of profiles, whereas almost all observations show a pure emission profile. Interestingly, both problems have also been found in analogue investigations by Jokuty (2002) performed by means of FASTWIND, an independent code that uses similar physics as

decribed here. Note particularly that optical analyses of a large sample of O-stars using the latter code gave no evidence of significant clumping effects for  $H\beta$  (cf. Repolust et al. 2004).

Thus, although clumping cannot be excluded, the degree of mismatch between synthetic and observed profiles and  $EW$ s indicates that some additional (physical) processes might be involved. Indeed, the difference between observed and synthesized profile shapes points to a line source function which should be closer to LTE than presently calculated (P Cygni shaped recombination lines can arise only due to departures from LTE, whereas LTE results in pure emission profiles, cf. Puls et al. 1996). Additionally, the sensitivity of the line source function on small changes in departure coefficients (see Eq. (3)) renders the possibility that the degree of mismatch is not as large as indicated on a first glance, and that some subtle modifications in the underlying physics might cure the problem. To this end, an update of presently used hydrogen line-collision rates as proposed by Butler & Przybilla (in preparation for A&A) might help in driving the transition closer to LTE and increasing the line emission.

Another evidence that the above problem is somewhat peculiar follows from the fact that the  $Br\alpha$  measurements appear to follow the predictions fairly well. If clumping would play a role in the formation of  $Br\gamma$ , this would suggest that the clumping factor varies throughout the wind, reaching a maximum in the lower wind regions and decreasing again farther out. Since  $Br\alpha$  originates in a larger volume of the wind, it would be relatively less affected by clumping.

#### 4.2. He II lines

Observations of the He II(7–12) and (7–10) lines are compared with predictions in the middle panel of Fig. 5. For the (7–12) line only few observations are available, limiting a meaningful comparison. For those few available data points, it appears that the models reproduce the observations reasonably well. A much better comparison can be made for the (7–10) line at  $\lambda 2.1891 \mu\text{m}$ . Though the observed global trends are recovered, we find that for dwarf stars with spectral types earlier than O7 this line is overpredicted by about  $0.5 \text{ \AA}$ , similar to the optical He II line. For supergiants of spectral type later than O6, the (7–10) line at  $\lambda 2.1891$  is underpredicted by up to  $\sim 1 \text{ \AA}$  for supergiants of spectral type later than O6. The reason for this behaviour is most likely linked to the uncertainty in the density structure. We find that the line cores of the He II lines are typically formed at 10 to  $100 \text{ km s}^{-1}$ , i.e., at or even beyond the sonic point. This implies that the dominant line contribution is formed in the transition region from the photosphere to the wind, for which we essentially do not have a self-consistent solution for the density structure (see Sect. 2.1). The results suggest that especially for supergiants the simple transition from an exponentially decaying density to that implied by a  $\beta$ -type velocity law adopted in our models is not correct (and not as much the simplified hydrostatic density structure in the photosphere itself).

#### 4.3. He I lines

For the He I lines a comparison of the  $\lambda 1.7007$ ,  $\lambda 2.1126$ , and  $\lambda 2.0587$  lines is feasible (right panel). Though

observational data is also available for the  $\lambda 3.7035 \mu\text{m}$  line, this data is limited to only a few stars. Moreover, our models do not account for the Stark broadening of this line. We therefore decided to exclude this line from the comparison. For the remaining three lines both the trend in spectral type and in luminosity class are reproduced by the predictions. In particular, the He I  $\lambda 2.1126$  line behaves well. Note that this 3p–4s transition is plotted as the sum of the  $\lambda 2.1126$  and  $\lambda 2.1138$  transitions, which are blended with each other in the medium resolution spectra of Hanson et al. (1996). Also the  $\lambda 2.0587$  line behaves well, though most supergiants appear to show a deeper absorption by up to  $\sim 1 \text{ \AA}$ . The same discrepancy for supergiants seems present in the  $\lambda 1.7007$  line. The cause of the systematic differences in absorption strength are again most likely connected to the density stratification in the transition from photosphere to wind.

We conclude from this comparison that the models reproduce the global trends of H (with severe problems in  $Br\gamma$ ), He I, and He II lines, but that the strength of helium lines tends to be underpredicted for the supergiants with spectral type later than O6. The models that best approach the He line strengths in Ia stars are the ones with low gravity, i.e. not with canonical values. This does not imply that these stars have a much lower mass than expected, but shows that the density structure in the transition region and lower wind is better represented by a low gravity in Eq. (2). We also like to remind the reader that all models have been calculated with normal helium abundance, which introduces additional uncertainties in those cases when the stellar atmosphere contains enhanced He, e.g. due to rotational mixing.

#### 4.4. Lines of carbon and nitrogen

The majority of the lines present in the near-infrared spectra of hot stars are produced by hydrogen and helium. In the  $K$  band, a few strong emission lines are attributed to carbon and nitrogen ions. A triplet of lines around  $2.08 \mu\text{m}$ , identified as the C IV (3p–3d) transitions, appear strongly in emission in the spectra of stars with spectral type O4 to O6.5. In our models, however, these lines are strongly in absorption at spectral types earlier than O5.5. They revert in emission only for later types and disappear at O9. It is obvious that our models fail in reproducing these transitions. Matching of the carbon lines is known to be problematic in O-type stars (e.g., Lamers et al. 1999) as a result of uncertainties in the ionization structure of this element. The carbon ionization is sensitive to the amount of line blanketing in the extreme ultraviolet (EUV) part of the spectrum, notably in the ionizing continua of C III and C IV. However, the  $2.08 \mu\text{m}$  C IV lines are observed to be narrow with a  $FWHM$  of about  $43 \text{ km s}^{-1}$  (Bik et al. in preparation) indicating that they originate in the photosphere and are not filled in by a contribution from the wind. A change in the abundance of C IV due to metallicity would influence the strength of the  $2.08 \mu\text{m}$  lines without reverting them into emission profiles. The formation region of the near-infrared C IV lines largely overlaps with that of the He I line at  $\lambda 2.0587 \mu\text{m}$ . Our models qualitatively reproduce the behaviour of the He I line indicating that the local

parameters in this region are most likely reasonable. The levels taking part in the C IV lines observed around  $2.08 \mu\text{m}$  are populated through transitions located in the EUV. The inclusion of Fe III, C III and O III had the direct consequence that the C IV lines reverted into emission in models with effective temperature from about 40 000 to 32 000 K. Though we account for approximately 30 000 lines (see Sect. 2), this does likely not yet represent all of the blanketing at EUV wavelengths. A more complete inclusion of EUV lines is currently under investigation and may further reduce the C IV discrepancy at temperatures higher than 40 000 K.

Our model atoms do not include data for N III (7–8), expected to be partly responsible for the observed emission near  $\lambda 2.1155 \mu\text{m}$ . Still, our predictions show an emission due to C III (7–8) at  $\lambda 2.1151 \mu\text{m}$ . The *EW* of this line peaks at  $0.8 \text{ \AA}$  for spectral type O6.5. This is much weaker (1 to 5  $\text{\AA}$ ) than observed, though it may explain some observations for spectral types O6 and later.

## 5. Diagnostics

In the Morgan & Keenan (MK, see Morgan & Keenan 1973) classification scheme stars of spectral type O are defined by the presence of He II lines. Subtypes are defined on the basis of the relative strength of the He I and He II lines. The luminosity class of O-type stars is based on optical Si IV and He I lines (e.g., Walborn 1990). A quantification of the spectral type calibration was proposed by Conti & Alschuler (1971), Bisiacchi et al. (1982) and Mathys (1988). In this section, we investigate the correlation between optical and near-infrared line ratios. This may lead to an extension of the quantitative spectral classification to near-infrared lines.

The advantage of the near-infrared spectral range over the optical is that it contains a range of hydrogen lines from different series and from high levels in the atom. Although this implies an additional diagnostic potential (see Lenorzer et al. 2002b), it does require spectra of sufficient quality, both in terms of signal-to-noise and spectral resolution, in order to capitalize on this. Also,  $\alpha$ ,  $\beta$ , and  $\gamma$  lines are stronger than their counterparts in the Balmer series in the optical. This may turn out to be beneficial, especially for wind density determinations based on Br $\alpha$  (see Sect. 5.3). The helium lines in the optical and near-IR are about equally strong, so in principle they may serve equally well for spectral classification. In practice the data quality is usually somewhat less in the near-IR as present day detectors for this wavelength regime have a poorer quantum efficiency than optical instruments do.

### 5.1. Spectral type

When correlating the optical and near-infrared line behaviour, we first notice that O-type stars are no longer *defined* by the presence of He II lines if one concentrates on only the near-infrared window. Indeed, at these wavelengths, most He II lines disappear around spectral type O8.5. Consequently, near-infrared He I/He II line ratios can only be measured for earlier spectral types. This is to be expected as the near-infrared

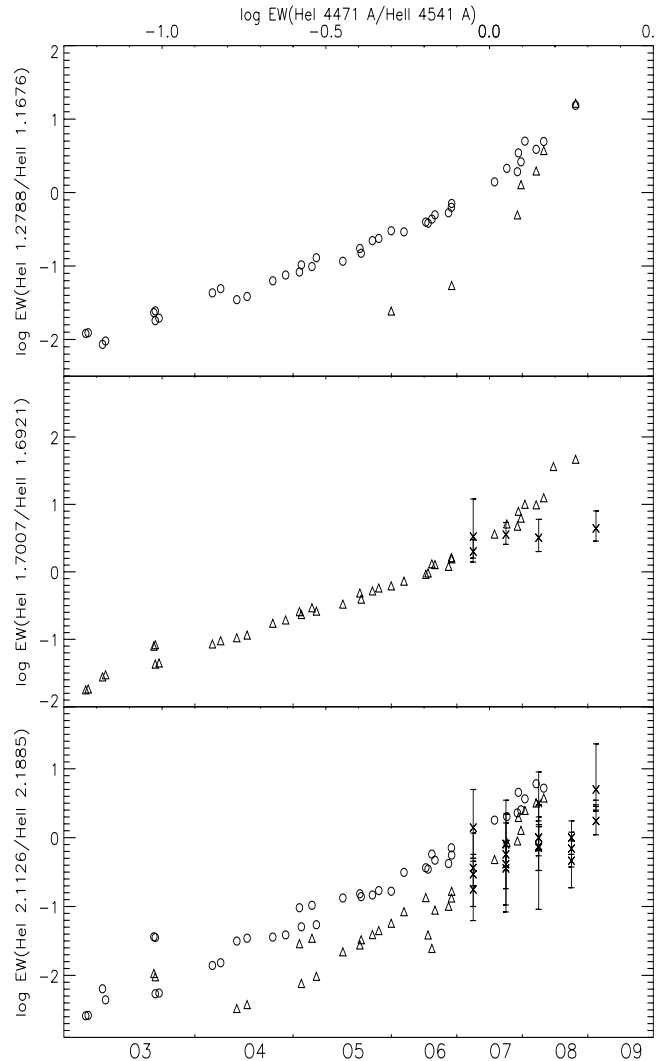


**Fig. 6.** The correlation between optical and near-infrared He I/He II equivalent width ratios which may be used to calibrate spectral types. Circles denote *EW* predictions for a relatively high spectral resolution ( $R \sim 4500\text{--}6000$ ); triangles give predictions for medium resolution ( $R \sim 1000$ ). The plus symbols give observed ratios.

continuum is formed further out in the atmosphere of O-type stars, where the temperature is lower.

Predicted He I/He II equivalent width ratios are presented in Fig. 6 for lines in the *J*, *H* and *K* band. In the *L*-band no suitable helium lines were found. No distinction between the luminosity classes was made and values applicable for both high- and medium-resolution spectra are plotted. High spectral resolution (circles in Fig. 6) implies  $R \sim 6500$  and 4500 for the *J* and *K* band. With medium resolution (triangles)  $R \sim 1000$  is implied. In the *J*-band (top panel) we find that the ratio He I  $\lambda 1.2788$ /He II  $\lambda 1.1676$  may serve to determine the spectral type. This only works at high resolution, as else the He I  $\lambda 1.2788$  line starts to blend with C III  $\lambda 1.2794$ , rendering this diagnostic unusable. Note that for He I  $\lambda 1.2788$  no Stark broadening is taken into account. This will affect the slope of the relation and at present prevents a reliable use of this ratio as a temperature diagnostic.

In the  $H$  band (middle panel) the best candidate line ratio for determining spectral type is He I  $\lambda 1.7007$  / He II  $\lambda 1.6921$ . In practice, the optical ratio He I  $\lambda 4471$  over He II  $\lambda 4542$  is found to be of practical use for ratios in between about  $-1$  and  $+1$  dex; otherwise one of the two lines gets too weak. The same applies to the identified  $H$  band ratio, implying that it can be used to determine the spectral type of O4 through O8 stars.

Overplotted in Fig. 6 are observed He I/He II ratios from Hanson et al. (1998) in the  $H$  band and from Hanson et al. (1996) in the  $K$  band. In the  $H$  band only few observations are available for spectral type O7 through O9. These seem to form an extension of the predicted slope that is found for stars of types O7 and earlier. However, at spectral type O8 the predicted curve turns upward, i.e. the models appear to overpredict the helium line ratio. In the  $K$  band, more data is available, although also only for types O7 and later as otherwise the He I  $\lambda 2.1126$  line is too weak to be measured. The available data is mainly for supergiants. We find that the observations extend the predictions of the low surface gravity models for stars of spectral type O7 or earlier, and underpredict the ionisation for cooler stars. On the basis of such a limited comparison it is difficult to draw firm conclusions. We again note that the observed ratios appear in better accordance with the low gravity models. This likely implies that for supergiants the density structure in the transition region and lower part of the wind connects more gradual (i.e. with a smaller density gradient) than is assumed in our standard supergiant grid, rather than that it implies an overestimate of the mass.

The predicted near-infrared equivalent width ratios presented in Fig. 6 correlate well with the optical ratio and show a steeper dependence on spectral type than does He I  $\lambda 4471$  over He II  $\lambda 4541$ . These near-infrared line ratio may serve to determine the spectral type. As for our model predictions, we note that the predictions for He I  $\lambda 1.2788$  do not account for Stark broadening effects. Therefore, the  $J$  band ratio is less steep than presented, yielding spectral types that are systematically too early. The  $H$ -band and  $K$ -band ratio are also to be taken with care as our models do not perfectly reproduce the observed line strengths (see Sect. 4). Still they give a reasonably good idea of the observational requirements needed to derive quantitative information on the spectral type of hot stars from near-infrared spectroscopy alone. We conclude that a derivation of the spectral sub-type of O stars from near-infrared helium line ratios is in principle feasible for good quality spectra in the  $J$ ,  $H$ , and  $K$  band and for stars that have spectral types in the range O4 to O8.

## 5.2. Surface gravity

Several of the strongest lines in the near-infrared, such as Br $\alpha$ , Bry, Pfy, and He II  $\lambda 3.0917$ , appear to be very sensitive to the surface gravity. This is, however, a consequence of the relation we assume between gravity and mass-loss rate. These lines are mainly formed in the wind and may serve as an indicator of the wind density (see next subsection).

The lines showing a direct dependence on surface gravity are the weaker lines, formed near the stellar photosphere. Most

He I and a few He II lines are found to be sensitive to this parameter. The He II (6–11), (7–10), (7–11) and (7–12) and the He I (2s–2p) lines are stronger in absorption for lower gravity at temperatures between 30 and 40 kK (see Sect. 3). The same holds for most He I lines between 25 and 35 kK. Unfortunately, no well defined monotonic correlation could be extracted.

## 5.3. Wind density

Mass-loss rates of O-type stars can be determined from ultraviolet resonance and subordinate lines, H $\alpha$ , and radio flux measurements. For a recent review on these methods, including a discussion of their individual pros and cons, see Kudritzki & Puls (2000). A relatively simple method to derive  $\dot{M}$  is to use the net equivalent width of H $\alpha$  (see e.g., Klein & Castor 1978; Leitherer 1988; Puls et al. 1996) and to correlate it with the equivalent width invariant

$$Q = \frac{\dot{M}}{R^{3/2} T_{\text{eff}}^2 v_{\infty}}, \quad (5)$$

first introduced by Schmutz et al. (1989) for a fixed temperature, and extended to include  $T_{\text{eff}}$  by Puls et al. (1996) and de Koter et al. (1998). The invariant essentially expresses that H $\alpha$  is formed by the recombination mechanism, therefore its strength will be approximately proportional to the mean column mass  $\bar{\rho}^2 R_{\star} \sim \dot{M}^2 / (R_{\star}^3 v_{\infty}^2)$ . In principle, the same strategy can be applied using the Br $\alpha$  line. Relations between the  $EW$  of Br $\alpha$  and the mass-loss rate have already been proposed, based on model predictions (Schaerer et al. 1996); and on observations (Lenorzer et al. 2002a). This line is intrinsically stronger than H $\alpha$ , which means that the photospheric absorption has a smaller impact on its  $EW$ . We have opted not to correct for a photospheric contribution, as a “true” photospheric component of this line can only be defined if a core-halo approximation is adopted (i.e. a separate treatment of the stellar photosphere and wind), which is not physically realistic in the near-infrared regime. Recall that most near-infrared lines are formed mainly in the transition region.

The correlation between predicted Br $\alpha$  equivalent width and  $Q$  is given in Fig. 7. The units of the constituents of the latter quantity are  $\dot{M}$  in  $M_{\odot} \text{ yr}^{-1}$ , stellar radius in  $R_{\odot}$ ,  $T_{\text{eff}}$  in Kelvin, and  $v_{\infty}$  in  $\text{km s}^{-1}$ . The measurements are from 4.0 to 4.1  $\mu\text{m}$  and include a number of blends from weak He I and He II lines. This causes most of the modest scatter in the model results; overall the correlation is very good. A best fit (overplotted using a solid line) to all negative  $EW$  values yields

$$\log EW(\text{Br}\alpha) = (32.4 \pm 0.5) + (1.55 \pm 0.03) \log Q. \quad (6)$$

The divergence from the fit of models with mass-loss rates below about  $10^{-7} M_{\odot} \text{ yr}^{-1}$  marks the transition to profiles dominated by photospheric absorption. In the wind dominated regime the fit function recovers the  $Q$  value to within 0.05 to 0.15 dex for  $0.5 < Q/10^{-20} < 1.0$ , and to within 0.04 dex for larger values. The reader may note that the above correlation has been evaluated for the models as described in Sect. 2, i.e. for a wind velocity law with  $\beta = 0.8$  and 1.0 for dwarfs

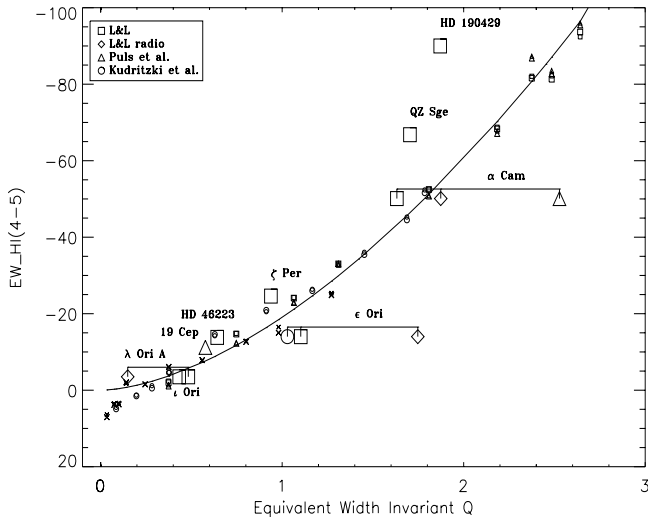


**Fig. 7.** The predicted equivalent widths for dwarfs (denoted by crosses), giants (circles) and supergiants (squares) and lower surface gravity supergiants (triangles) are overplotted with observations from Lenorzer et al. (2002a), for which  $Q$  was derived from Lamers et al. (1999), Puls et al. (1996), and Kudritzki et al. (1999).  $Q$  is given in units of  $10^{-20} M_{\odot} \text{ yr}^{-1} \text{ per } R_{\odot}^{3/2} \text{ per } \text{K}^2 \text{ per } \text{km s}^{-1}$ .

and supergiants, respectively. Since  $\text{Br}\alpha$  is strongly density dependent, different values for  $\beta$  will introduce certain deviations from this relation (cf. Puls et al. 1996).

In Fig. 7 we overplot the observed equivalent widths of nine giants and supergiants. The  $Q$  values corresponding to these  $EW$  are from Puls et al. (1996), Lamers et al. (1999) and Kudritzki et al. (1999) (see figure caption for details). The bars connect mass-loss determinations for the same stars by different authors, sometimes using different methods ( $\text{H}\alpha$  or radio). The bars therefore give an indication of the uncertainties involved in deriving  $\dot{M}$ . Typical errors on individual measurements are about 0.3 dex in the  $Q$  parameter. In seven out of nine cases the determinations are in good agreement with the trend. This ignores the outlying  $\dot{M}$  results for  $\alpha$  Cam and  $\epsilon$  Ori. The observed  $EW$  for the two Iaf supergiants in the sample, HD 190429A and QZ Sge, are clearly above the trend. These two stars show He II emission lines that are much stronger than the ones produced in our supergiant models. One of these He II lines is included in the measurement of the  $\text{Br}\alpha$  equivalent width, explaining the difference.

## 6. Conclusions

We have confronted observations of near-infrared spectra with predictions using the current state-of-the-art model atmosphere code CMFGEN of Hillier & Miller (1998). This study was prompted by the fact that an increasing number of spectra of embedded O-type stars is presently becoming available, allowing the study of stars hidden beyond tens of magnitudes of circumstellar or foreground visual extinction. Though first attempts to make an inventory of the potential and predictive power of models in this wavelength range have been undertaken (Najarro et al. 1999), a systematic approach using a large

grid of models was so far missing. We summarize the main conclusions of this study.

1. The general trends and strengths of the lines are fairly compatible with observed properties. Near-infrared lines are typically formed in the transition region from photosphere to stellar wind, or even in the lower part of the wind (up to a few times the sonic velocity). The largest discrepancies are found for helium lines in supergiant spectra, which are systematically underpredicted. As low gravity models appear to reproduce these lines much better, it is expected that for these stars the connection of the photosphere to the wind is much smoother, i.e. the density changes more gradually, than is adopted in our models. (It does not imply that masses for supergiants are systematically underestimated.)
2. The models show a good correlation between optical and near-infrared helium line ratios in the  $J$ ,  $H$  and  $K$  band. Notably, the  $\text{He I } \lambda 1.2788 / \text{He II } \lambda 1.1676$ ,  $\text{He I } \lambda 1.7007 / \text{He II } \lambda 1.6921$ , and  $\text{He I } \lambda 2.1136 / \text{He II } \lambda 2.1885 \mu\text{m}$  ratios appear good candidates. Application of these near-infrared ratios requires good quality data and are only applicable for stars with spectral type O4 to O8. Cooler stars do not show He II lines. This is to be expected as the near-infrared continuum is formed further out in the atmosphere, relative to where the optical spectrum originates.
3. The  $\text{Br}\alpha$ ,  $\text{Br}\gamma$ , and  $\text{He II } \lambda 3.0917$  lines in giants and supergiants are predominantly formed in the stellar wind. Comparison with observations shows that the  $\text{Br}\gamma$  lines are systematically underpredicted, while in most cases  $\text{Br}\alpha$  is reproduced well. We have argued that  $\text{Br}\gamma$  might be affected by an inhomogeneous density distribution or “clumping”, while the stronger  $\text{Br}\alpha$  line suffers much less from this effect, which would suggest a distance dependent clumping. Additional arguments concerning line formation depth and profile shape of  $\text{Br}\gamma$ , however, point also to presently unknown processes which have to be identified in future investigations.
4. We find that the  $\text{Br}\alpha$  line is a fairly good diagnostic for the wind density and we provide a means to correlate the measured equivalent width of this line to the wind density invariant  $Q = \dot{M} / R^{3/2} v_{\infty} T_{\text{eff}}^2$ . The relation, however, depends on the He II abundance in the wind, as the  $\text{Br}\alpha$  line is contaminated by a potentially strong He II line and may strongly affect mass loss predictions for Iaf stars.

*Acknowledgements.* The authors are very grateful to D. J. Hillier who courteously provided his CMFGEN code, as well as help in setting up the grid. We would like to thank F. Najarro for inspiring and constructive discussions and D. Schaerer whose careful reading and suggestions helped improving the quality of this paper. We also wish to thank the referee A. Herrero for his critical reading and constructive comments.

## References

- Abbott, D. C. 1982, *ApJ* 259, 282  
 Blum, R. D., Ramond, T. M., Conti, P. S., Figer, D. F., & Sellgren, K. 1997, *AJ*, 113, 1855

- Bisiacchi, G. F., Lopez, J. A., & Firmani, C. 1982, *A&A*, 107, 252
- Bouret, J.-C., Lanz, T., Hillier, D. J., et al. 2003, *ApJ*, 595, 1182
- Castor, J. I., Abbott, D. C., & Klein, R. K. 1975, *ApJ*, 195, 157
- Conti, P. S., & Alschuler, W. R. 1971, *ApJ*, 170, 325
- Conti, P. S., & Frost, S. A. 1977, *ApJ*, 212, 728
- Cox, A. N. 2000, *Allen's astrophysical quantities*, 100, 72
- Crowther, P. A., Hillier, D. J., & Smith, L. J. 1995, *A&A*, 293, 172
- de Koter, A., Heap, S. R., & Hubeny, I. 1998, *ApJ*, 509, 879
- Eversberg, T., Lepine, S., & Moffat, A. F. J. 1998, *ApJ*, 494, 799
- Groenewegen, M. A. T., & Lamers, H. J. G. L. M. 1989, *AAS*, 79, 359
- Hanson, M. M., Conti, P. S., & Rieke, M. J. 1996, *ApJS*, 107, 281
- Hanson, M. M., Rieke, G. H., & Luhman, K. L. 1998, *ApJ*, 116, 1915
- Hanson, M. M., Luhman, K. L., & Rieke, G. H. 2002, *ApJS*, 138, 35
- Hanson, M. M., Kaper, L., Bik, A., et al. 2003, ed. K. A. van der Hucht, A. Herrero, & C. Esteban, *Proc. IAU Symp.*, 212, *ASP Conf. Ser.*, 467
- Herrero, A., Kudritzki, R. P., Vilchez, J. M., et al. 1992, *A&A*, 261, 209
- Hillier, D. J. 1991, *A&A*, 247, 455
- Hillier, D. J., & Miller, D. L. 1998, *ApJ*, 496, 407
- Jokuthy, A. 2002, *Infrared spectral analysis of hot stars*, Diploma Thesis, University of Munich
- Kaper, L., Bik, A., Hanson, M. M., & Comerón, F. 2002, in *Hot Star Workshop III: The Earliest Stages of Massive Star Birth*, *ASP Conf. Proc.*, 267, 95
- Kendall, T. R., de Wit, W. J., & Yun, J. L. 2003, *A&A*, 408, 313
- Klein, R. I., & Castor, J. I. 1978, *ApJ*, 220, 902
- Kudritzki, R. P. 1979, *Proc. 22nd Liège Int. Symp.*, 295
- Kudritzki, R.-P., Puls, J., & Lennon, D. J. 1999, *A&A*, 350, 970
- Kudritzki, R.-P., & Puls, J. 2000, *ARA&A*, 38, 613
- Lamers, H. J. G. L. M., Snow, T. P., & Lindholm, D. M. 1995, *ApJ*, 455, 269
- Lamers, H. J. G. L. M., Haser, S., de Koter, A., & Leitherer, C. 1999, *ApJ*, 516, 872
- Leitherer, C. 1988, *ApJ*, 326, 356
- Lenorzer, A., Vandenbussche, B., Morris, P., et al. 2002a, *A&A*, 384, 473
- Lenorzer, A., de Koter, A., & Waters, L. B. F. M. 2002b, *A&A*, 386, L5
- Lucy, L. B. 1976, *ApJ*, 205, 482
- Martins, F., Schaerer, D., & Hillier, D. J. 2002, *A&A*, 382, 999
- Mathys, G. 1988, *A&AS*, 76, 427
- Mathys, G. 1989, *A&AS*, 81, 237
- Mihalas, D. 1978, *Stellar Atmospheres* (San Francisco: Freeman), 2nd edition
- Morgan, W. W., & Keenan, P. C. 1973, *ARA&A*, 11, 29
- Najarro, F., Hillier, D. J., Kudritzki, R. P., et al. 1994, *A&A*, 285, 573
- Najarro, F., Hillier, D. J., & Stahl, O. 1997, *A&A*, 326, 111
- Najarro, F., Kudritzki, R. P., Hillier, D. J., et al. 1998, *Proc. 2nd Boulder-Munich Workshop, PASP*, 131, 57
- Najarro, F., Hillier, D. J., Kudritzki, R. P., & Morris, P. W. 1999, in *The Universe as Seen by ISO, ESA-SP*, 427, 377
- Owocki, S. P., Castor, J. I., & Rybicki, G. B. 1988, *ApJ*, 335, 914
- Owocki, S. P., & Puls, J. 1999, *ApJ*, 510, 3550
- Pauldrach, A. W. A., Puls, J., & Kudritzki, R. P. 1986, *A&A*, 164, 86
- Puls, J., Kudritzki, R.-P., Herrero, A., et al. 1996, *A&A*, 305, 171
- Repolust, T., Puls, J., & Herrero, A. 2004, *A&A*, 415, 349
- Robert, C. 1994, *A&ASS*, 221, 137
- Schaerer, D., de Koter, A., Schmutz, W., & Maeder, A. 1996, *A&A*, 312, 475
- Schaller, G., Schaerer, D., Meynet, G., & Maeder, A. 1992, *A&AS*, 96, 269
- Schmutz, W., Hamann, W.-R., & Wessolowski, U. 1989, *A&A*, 210, 236
- Smith, K. C., & Howarth, I. D. 1998, *MNRAS*, 299, 1146
- Vacca, W. D., Garmany, C. D., & Shull, J. M. 1996, *ApJ*, 460, 914
- Villamariz, M. R., & Herrero, A. 2000, *A&A*, 357, 597
- Vink, J. S., de Koter, A., & Lamers, H. J. G. L. M. 2000, *A&A*, 362, 295
- Vink, J. S., de Koter, A., & Lamers, H. J. G. L. M. 2001, *A&A*, 369, 574
- Walborn, N. R., & Fitzpatrick, E. L. 1990, *PASP*, 102, 379
- Wallace, L., & Hinkle, K. 1997, *ApJS*, 111, 445
- Zaal, P. A., de Koter, A., Waters, L. B. F. M., et al. 1999, *A&A*, 349, 573
- Zaal, P. A., de Koter, A., & Waters, L. B. F. M. 2001, *A&A*, 366, 241